Effect of system compliance on weld power in ultrasonic additive manufacturing

Gowtham Venkatraman

Department of Mechanical and Aerospace Engineering, The Ohio State University, Columbus, Ohio, USA

Adam Hehr

Fabrisonic LLC, Columbus, Ohio, USA, and

Leon M. Headings and Marcelo J. Dapino

Department of Mechanical and Aerospace Engineering, The Ohio State University, Columbus, Ohio, USA

Abstract

Purpose – Ultrasonic additive manufacturing (UAM) is a solid-state joining technology used for three-dimensional printing of metal foilstock. The electrical power input to the ultrasonic welder is a key driver of part quality in UAM, but under the same process parameters, it can vary widely for different build geometries and material combinations because of mechanical compliance in the system. This study aims to model the relationship between UAM weld power and system compliance considering the workpiece (geometry and materials) and the fixture on which the build is fabricated.

Design/methodology/approach – Linear elastic finite element modeling and experimental modal analysis are used to characterize the system's mechanical compliance, and linear system dynamics theory is used to understand the relationship between weld power and compliance. In-situ measurements of the weld power are presented for various build stiffnesses to compare model predictions with experiments.

Findings – Weld power in UAM is found to be largely determined by the mechanical compliance of the build and insensitive to foil material strength. **Originality/value** – This is the first research paper to develop a predictive model relating UAM weld power and the mechanical compliance of the build over a range of foil combinations. This model is used to develop a tool to determine the process settings required to achieve a consistent weld power in builds with different stiffnesses.

Keywords Advanced manufacturing technologies, Metals, Modeling, Ultrasonic additive manufacturing (UAM), Advanced manufacturing, Process modeling, In-situ measurements, LTI model

Paper type Research paper

1. Introduction

Ultrasonic additive manufacturing (UAM), or ultrasonic consolidation, is a solid-state process capable of producing gapless metal three-dimensional printed parts (Graff et al., 2010). The process works by welding together similar or dissimilar metal foils in an additive fashion using ultrasonic welding. The ultrasonic welder is integrated into a computer numerical control (CNC) framework to permit intermittent machining between welding operations. The subtractive feature of the process enables the fabrication of complex internal features, embedment of objects, and net shaping of parts (White, 2003). The state-of-the-art UAM system used in this paper, a Fabrisonic 9 kW SonicLayer 4000, is shown in Figure 1, which illustrates the additive and subtractive stages of the process.

The welding or additive stage of the process works by bringing a tool piece called the sonotrode or horn into contact with a metallic foil under controlled pressure. Then, the sonotrode is actuated at a nominal resonance frequency of 20 kHz with piezoelectric transducers, which scrubs the

The current issue and full text archive of this journal is available on Emerald Insight at: https://www.emerald.com/insight/1355-2546.htm



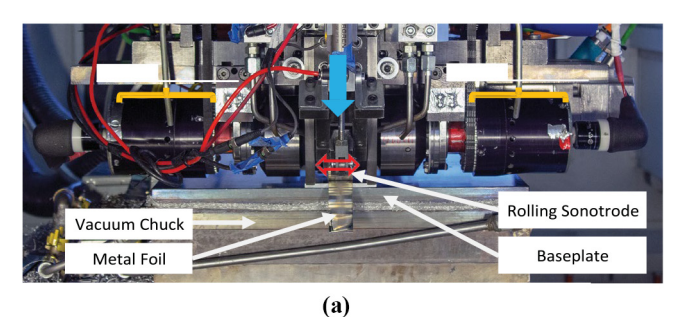
metallic foil against pre-deposited metal foils or a baseplate metal beneath. The circular design of the sonotrode allows it to rotate at a prescribed speed while welding.

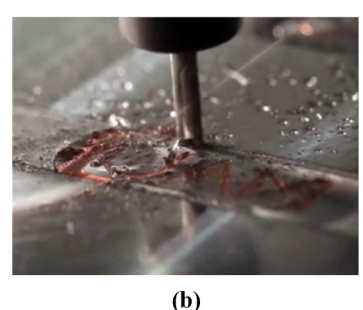
A key feature of the UAM process is the low formation temperature, which enables the joining of dissimilar metals without the formation of brittle intermetallic phases. The low temperature aspect of the process enables the joining of many different metal combinations (Obielodan *et al.*, 2010). Using thermocouples embedded at the weld interface, Sriraman *et al.* (2011) showed that the peak temperature reaches near 150 °C for welding aluminum and copper alloys with a 9 kW welder. Intermetallics often form in fusion processes with dissimilar metals because elevated temperatures permit mixing and diffusion. In contrast, melting and subsequent solidification are absent in UAM, and diffusion is minimal.

This material is based upon work supported by the National Science Foundation, CMMI Division Grant No. 1538275. G.V. was supported from a NSF Graduate Fellowship under Grant No. 1102690 and from the member organizations of the Smart Vehicle Concepts Center (www. SmartVehicleCenter.org), a National Science Foundation Industry/University Cooperative Research Center. Any opinions, findings, and conclusions or recommendations expressed in this material are those of the authors and do not necessarily reflect the views of the National Science Foundation.

Received 21 July 2020 Revised 24 January 2021 25 April 2021 Accepted 26 April 2021

Figure 1 Fabrisonic 9 kW SonicLayer 4000 ultrasonic additive manufacturing system: (a) the ultrasonic welder is used to additively join foils together on a steel vacuum chuck fixture; (b) the subtractive CNC stage is used to introduce complex internal features and to trim components. The two Dukane ultrasonic transducers are each rated to 4.5 kW. The solid blue downward arrow represents the normal force applied during welding (weld force) and the hollow red side-to-side arrow represents the vibratory scrubbing action





The introduction of very high power UAM, which increased the power envelope of the process from 1 kW in first-generation systems to 9 kW by using two piezoelectric transducers in a pushpull configuration, dramatically increased process capabilities to enable gapless, fully dense joints (Graff et al., 2011). The higher available weld power expands the range of alloys that can be welded with UAM: from softer 3000 series aluminum (Kong et al., 2004) to higher strength materials such as 6000 series aluminum (Wolcott et al., 2014), steel (Han et al., 2020) and titanium (Sridharan et al., 2016). Many UAM studies have been conducted to determine the optimal process parameters such as welder's vibration amplitude, travel speed of the welder (weld speed), weld force and baseplate temperature to produce strong welds between similar and dissimilar materials (Friel, 2015). However, the same process parameters produce different amounts of weld power depending on the workpiece geometry and the materials being welded, and these studies do not report weld power measurements. Weld power has been shown to have a strong influence on the mechanical strength and the microstructure of the weld interface (Hehr et al., 2016); therefore, it is necessary to develop a model for weld power as a function of process parameters and the geometry and material properties of the workpiece.

Hehr et al. (2016) showed that using a constant weld amplitude to weld all the layers of a 20-layer build using Al 6061-H18 results in a decrease in weld power with build height. The microstructure and strength of this so-called uncompensated build were compared with a build where the weld amplitude was increased with build height to maintain a constant weld power. The uncompensated build with lower weld power, and hence lower input strain energy, was found to have poor mixing and lower grain refinement than the power-compensated build. An 18% lower energy absorption and 6% lower peak force were also observed in push-pin testing of the uncompensated build. This showed a direct connection between the weld power in UAM to the weld interface microstructure and the mechanical strength of the resulting part. The structural compliance of the build has been shown to influence the weld power and the lateral compliance of the welded stack can be approximated using the expression for a cantilever beam fixed on one end. However, this work did not examine the effect of build geometry, foil materials being welded or establish a quantitative relationship between the system's compliance and weld power. Yi et al. (2017) studied the effect of build height on weld power using multiple regression analysis and developed an empirical fit between build height and weld power, but did not develop a physical model to predict weld power for an arbitrary workpiece geometry.

Hehr and Dapino (2017) developed a lumped parameter linear time invariant (LTI) model of the weld assembly, which relates the shear force and current to the voltage and vibration velocity. They proposed that this model, coupled with a complex stiffness load impedance term to model the dynamics of the workpiece, would be able to describe the transfer of power from the weld assembly to the workpiece during UAM. Viscous damping elements can be used to model a range of loss mechanisms such as hysteretic damping or Coulomb friction (de Silva, 2007). Networks of viscous damping and spring elements have been used in modeling the dynamics of tool-workpiece interactions in other manufacturing processes, including ultrasonic (Wiercigroch et al., 1999), ultrasonic machining (Wang and Rajurkar, 1996) and peripheral milling (Diez et al., 2017).

The broad objective of this paper is to establish a relationship between the mechanical compliance of the build (which includes the foil material being welded, the workpiece being welded onto and the fixture) and weld power. Because a change in power is observed to have a significant effect on weld quality (Hehr et al., 2016), the goal of this investigation is to develop a predictive tool to determine the weld parameter settings needed to obtain a target weld power for UAM joining of metals with different build configurations. The travel speed of the welder (weld speed) is fixed in this analysis, as previous works have found that changing the weld speed does not significantly change the weld power (Yi et al., 2017). Preheating has been used in UAM to improve bond quality (Han et al., 2020), but it is not used in this study, as it is not required for producing successful bonding for the materials tested.

In Section 2, a dynamic stiffness model is used to characterize the mechanical loading on the welder during UAM. This model is coupled with the LTI model of the weld assembly presented in Hehr and Dapino (2017) to develop an expression for weld power as a function of load stiffness. In Section 3, equivalent circuit analysis is used to develop a lumped parameter model for the dynamic load stiffness with a damping element in parallel with lumped compliance elements that account for the individual contributions from the foil being welded, welded stack, baseplate and fixture. Using

relationships developed in Section 2, weld power-stiffness relationships are developed. In Section 4, the stiffness of the foil with the workpiece (baseplate and welded stack) is characterized using finite element modeling (FEM). Modal analysis is used to characterize the stiffness of the steel vacuum chuck fixture.

In Section 5, three different studies are presented to test the weld power predictions for a range of workpiece and fixture configurations. The first study (Section 5.1) investigates the effect of baseplate stiffness on weld power by welding Al foil on Al and steel baseplates chosen with different stiffness values. The weld power predictions from the model show good agreement with these measurements. The second study (Section 5.2) investigates the effect of foil material stiffness on weld power using a stiffer foil material, copper. In total, 10 layers of Cu C11000-O60 were built onto an Al 6061-T6 baseplate, and the weld power measurements were compared with model predictions. The third study (Section 5.3) investigates the dependency of the parameters of the weld power model on the foil type. Al 6061-H18, Al 6061-O, Al 3003-H18 foils were chosen to be welded onto an Al 6061-T6 baseplate because they have the same elastic properties but very different characteristics in the plastic deformation regime. Cu C11000-O60 foils were also welded for comparison. It is observed that the model's damping parameter is not foildependent. The foils were also welded using a range of weld amplitudes to validate the weld power model.

2. Model for dynamic load stiffness and weld power in ultrasonic additive manufacturing

The LTI model of the weld assembly from Hehr and Dapino (2017), which relates the shear force and electric current to resultant welder velocity and voltage, is reproduced below with \dot{x}_{welder} replacing $\dot{\delta}$:

$$\begin{pmatrix} V(j\omega) \\ \dot{x}_{welder}(j\omega) \end{pmatrix} = \begin{bmatrix} H_e^*(j\omega) & H_{me}^*(j\omega) \\ H_{em}^*(j\omega) & H_m^*(j\omega) \end{bmatrix} \begin{pmatrix} i(j\omega) \\ F_s(j\omega) \end{pmatrix}. \tag{1}$$

This model describes the interrelation between the electrical and mechanical signals in the frequency domain to explain the transfer between electrical and mechanical power within the welder. The terms $H_e^*(j\omega)$, $H_m^*(j\omega)$ and $H_{\rm me}^*(j\omega)$ are the electrical, mechanical and electromechanical transfer functions, respectively. The electrical signals $V(j\omega)$ and $i(j\omega)$ are the voltage and current applied to the transducers, respectively, and the mechanical signals $F_s(j\omega)$ and $\dot{x}_{\rm welder}(j\omega)$ are the shear force acting on the sonotrode and vibration velocity of the welder, respectively.

A dynamic mechanical stiffness term is used to model the load on the welder during UAM, which is then coupled with the LTI model of the weld assembly from Hehr and Dapino (2017). The parameterization of the dynamic stiffness term is discussed in Section 3, where we develop a relationship for weld power as a function of a generalized dynamic mechanical stiffness $\tilde{K}_{LD}(j\omega)$ that accounts for contributions from the contact interactions between the welder and the materials being welded. A parametric model for the load stiffness is then

developed by considering the individual contributions from the foil being welded, welded stack, baseplate and fixture.

The dynamic mechanical stiffness $\tilde{K}_{LD}(j\omega)$ is defined as the ratio of the shear force to the welder's vibration displacement. The stiffness can be separated into its real $(\tilde{K}_R(j\omega))$ and imaginary $(\tilde{K}_I(j\omega))$ parts as:

$$\tilde{K}_{LD}(j\omega) = \frac{F_s(j\omega)}{\dot{x}_{welder}(j\omega)/j\omega} = \tilde{K}_R(j\omega) + j\tilde{K}_I(j\omega). \tag{2}$$

The $(j\omega)$ term is dropped henceforth, for brevity. When the welder is under load, the relationships between the inputs and outputs in the electromechanical model at the excitation frequency can be simplified to the following expressions using \tilde{K}_{LD} as described in equation (2):

$$V = H_e^* i - H_{me}^* (\tilde{K}_R + j\tilde{K}_I) \frac{\dot{x}_{volder}}{j\omega}, \tag{3}$$

$$\dot{x}_{welder} = H_{em}^* i - H_m^* (\tilde{K}_R + j\tilde{K}_I) \frac{\dot{x}_{welder}}{j\omega}.$$
 (4)

Eliminating \dot{x}_{welder} from the two expressions, the relationship between voltage and current simplifies to:

$$\frac{i}{V} = \frac{1}{\Psi_t^2} \cdot \left(\left(D_t + \frac{\tilde{K}_I}{\omega} \right) + j \left(\omega M_t - \frac{K_t + \tilde{K}_R}{\omega} \right) \right), \tag{5}$$

where Ψ_{tr} M_{t} and D_{t} are the electromechanical transformer coefficient, effective mass and effective damping parameters of the LTI model for the weld assembly as defined in Hehr and Dapino (2017).

The welder is operated using a motional feedback controller, which uses a phase-locked loop algorithm that controls the operating frequency to minimize the phase difference between the voltage and current. This ensures that the voltage and current signals are in phase. As the voltage and current signals are in phase, the fundamental frequency of vibration of the welder during welding (f_{weld}) can be obtained from the angular frequency (ω_{weld}) by setting the imaginary part in the right-hand side of equation (5) to zero, giving:

$$f_{weld} = \frac{\omega_{weld}}{2\pi} = \frac{1}{2\pi} \sqrt{\frac{K_t + \tilde{K}_R}{M_t}}.$$
 (6)

The welder also uses amplitude control to keep the amplitude of the voltage constant during welding. Assuming harmonic signals V and i, the average electrical power consumed during welding can thus, be expressed as:

$$P_{e,avg}^{weld} = \frac{1}{2} |V| \cdot |i| = \frac{1}{2} |V|^2 \cdot \left| \frac{i}{V} \right| = \frac{1}{2} \left(D_t + \frac{\tilde{K}_I}{\omega_{weld}} \right) \frac{|V|^2}{\Psi_t^2}$$
$$= \frac{1}{2} \left(D_t + \frac{\tilde{K}_I}{\omega_{weld}} \right) |\dot{x}_{welder}|^2, \tag{7}$$

where $\left|V\right|$ and $\left|i\right|$ denote the zero-to-peak amplitudes of the respective signals.

3. Lumped parameter modeling of dynamic load stiffness

3.1 Equivalent circuit analysis

Figure 2(a) illustrates the components that contribute to the total system stiffness and how system stiffness impacts the UAM process. Because of the combined compliance of the UAM stack, the baseplate near the stack and the vacuum chuck, only a portion of the displacement imparted by the sonotrode is used to displace the new foil being welded relative to the stack. Figure 2(b) shows an electrical equivalent circuit representation of this system. This model is an extension of the equivalent circuit analysis of the weld assembly in Hehr and Dapino (2017). A viscous damping element, D_{loss} , is used to represent the mechanical losses in the weld zone. Lumped compliance elements are used to model the dynamic response of the foil, stack, baseplate and vacuum chuck fixture. System compliance is defined as the capacitance of the equivalent element in Figure 2(b), which is the effective stiffness of the parallel connection of capacitors. This gives the following expression for the effective system compliance as the reciprocal of the effective system stiffness K_{system} :

$$\frac{1}{K_{system}} = \frac{1}{K_{foil}} + \frac{1}{K_{stack}} + \frac{1}{K_{base}} + \frac{1}{K_{chuck}}.$$
 (8)

All the stiffness terms in the rest of this paper are in the lateral (along the welder's vibration) direction. The CNC table is modeled as a rigid base, hence its stiffness is assumed to be infinite [1]. The lumped stiffness of the vacuum chuck is estimated using modal analysis, detailed in Section 4.1. The stiffness of the foil, stack and baseplate are estimated using finite element analysis in Section 4.2.

For the equivalent circuit representation to be accurate, the following assumptions are made. First, it is assumed that there is no slip between the welder and new foil, and between the new foil and workpiece. The no-slip assumption is supported by findings in Sriraman et al. (2011), where good agreement was found between the temperature at the foil-to-foil interface measured using a thermocouple, and the temperature predicted using a thermal model that considered only plastic deformation as the heat source and neglected frictional slip. As detailed in Sriraman et al. (2011), while there is some work in the literature that does not neglect the contribution of frictional slip to the overall heating in ultrasonic welding, it is proposed that once initial sliding disperses the oxide layers and initiates the contact of nascent metal from both foils, there is no further slip at the weld interface.

Second, it is assumed that the dynamics of the workpiece are primarily influenced by its quasi-static stiffness. Lumped stiffness elements are thus used to approximate the dynamic response of the welded stack and baseplate. This assumption is valid if the frequency corresponding to the lateral (shear) mode of vibration of the structure is significantly higher than the excitation frequency of 20 kHz. The resonance frequency of the build can approach the excitation frequency of the welder (Gibert et al., 2010), which would affect the dynamic response of the build to sonotrode vibrations. An eigenfrequency analysis of a representative UAM build, a 20-layer Al stack welded onto a 9.53 mm (0.375 in) thick Al baseplate, was performed using COMSOL to estimate the frequency of the first shear mode. The first shear mode of vibration is shown in Figure 3, computed using the eigenfrequency solver within COMSOL. The eigenfrequency or resonant frequency of the stack and baseplate in shear is near 70 kHz, which is well above the excitation frequency of 20 kHz. As a result, the dynamics of the stack are primarily influenced by the quasi-static stiffness at 20 kHz. Hence, the system is assumed to be quasi-static for modeling purposes, and mass terms are not considered for the stack, foil or baseplate.

Third, it is assumed that the lumped viscous damping element in the weld zone in Figure 2(b) accounts for all of the energy losses near the horn-foil contact, including frictional

Figure 2 UAM stack and system dynamics: (a) schematic illustration of the components that contribute to the mechanical compliance of the system; (b) equivalent circuit representation of the system. The weld zone deformation is modeled using a viscous damping element

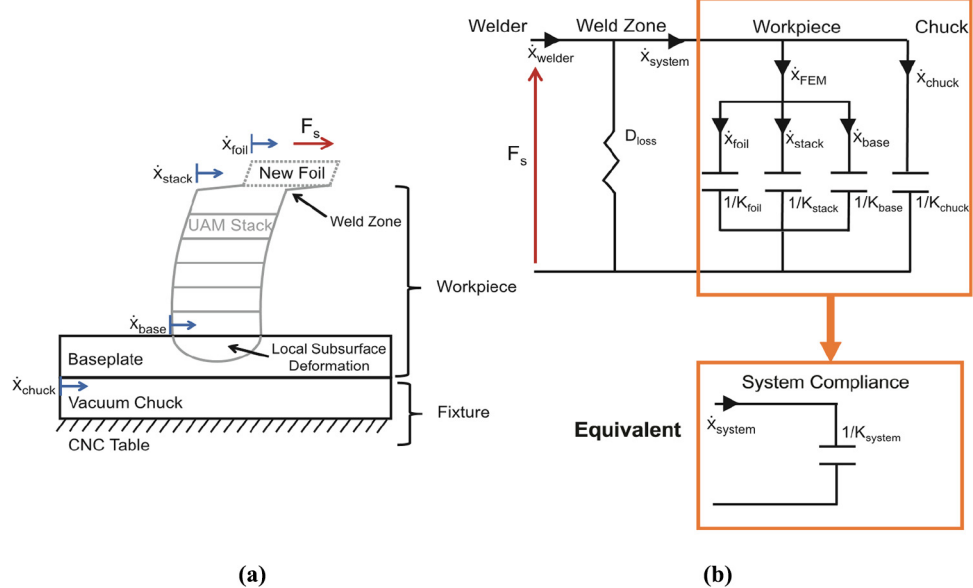
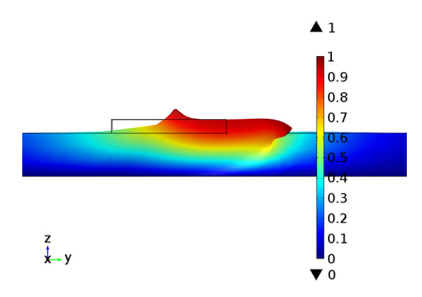


Figure 3 The first mode of vibration in shear of a 20-layer Al stack and 9.53 mm (0.375 in) thick Al baseplate in shear is identified using the eigenfrequency solver within COMSOL to be 70.4 kHz, which is well above the 20 kHz excitation frequency. The color scale represents the normalized total displacement



heating and plastic deformation near the weld interface. Losses due to friction in the baseplate and chuck are assumed to be negligible. The damping coefficient D_{loss} is assumed to be constant and not dependent on the weld parameters or foil type. This assumption is tested in Section 5.3.

3.2 Weld power - stiffness relationships

The average mechanical power consumption is affected by the phase angle between the harmonic shear force F_s and the welder's vibration velocity \dot{x}_{welder} , which changes when the system stiffness K_{system} is varied. The dynamic mechanical stiffness \tilde{K}_{LD} at the operating frequency is determined considering the system's compliance in parallel to the damping element, which has an impedance of $j\omega D_{loss}$, to be:

$$\tilde{K}_{LD}(j\omega_{veld}) = \frac{j\omega_{veld}}{(j\omega_{veld})/K_{system} + 1/D_{loss}},$$
(9)

$$=K_{\text{system}}\frac{\left(\omega_{\text{weld}}D_{\text{loss}}\right)^{2}}{K_{\text{system}}^{2}+\left(\omega_{\text{weld}}D_{\text{loss}}\right)^{2}}+j\omega_{\text{weld}}D_{\text{loss}}\frac{K_{\text{system}}^{2}}{K_{\text{system}}^{2}+\left(\omega_{\text{weld}}D_{\text{loss}}\right)^{2}},$$
(10)

where $\omega_{weld} = 2\pi f_{weld}$ and f_{weld} is the fundamental frequency of the welder's vibration velocity during welding, identified from equation (6).

Using the expression for weld power [equation (7)], and substituting $|\dot{x}_{welder}| = \omega |x_{welder}|$ in equation (10), the expression for weld power becomes:

$$P_{e,avg}^{weld} = \frac{1}{2} \left(D_t + D_{loss} \frac{K_{system}^2}{K_{system}^2 + (\omega_{weld} D_{loss})^2} \right) \omega_{weld}^2 |x_{welder}|^2.$$
(11)

This equation (11) is a non-linear relationship between the weld power and the system stiffness with tunable parameter D_{loss} to be determined from experimental data. This relationship indicates that there is a maximum attainable weld power for a given configuration of foils, computed by setting $K_{system} \rightarrow \infty$, which is $P_{e,avg}^{weld,max} = (D_t + D_{loss})\omega_{weld}^2|x_{welder}|^2/2$. The lowest value is attained when the welder is ringing in air, with $K_{system} = 0$, where $P_{e,avg}^{weld,min} = D_t \omega_{weld}^2|x_{welder}|^2/2$.

For a given weld speed, increasing weld power has been shown in the literature to produce UAM builds with improved mechanical strength (Hehr et al., 2016). Increasing weld amplitude ($|x_{welder}|$) results in a significant increase in weld power because of the quadratic relationship [equation (11)]. There are limits to increasing the power using this method due to the maximum voltage limit of the transducers. The weld power stiffness relationship [equation (11)] provides a framework for designing the workpiece being welded onto and the fixture to obtain higher weld power values for a given weld amplitude. Increasing the system stiffness K_{system} increases the weld power, but beyond the inflection point (the point where the second derivative of power with respect to stiffness is zero) $K_{system} = D_{loss} \omega_{weld} / \sqrt{3}$, increasing it leads to diminishing returns in weld power. This can be seen from the derivative of the weld power with respect to system stiffness, which decreases to zero as $K_{system} \rightarrow \infty$:

$$\frac{dP_{e,avg}^{vold}}{dK_{system}} = \quad \left(D_{loss} \frac{\left(\omega_{vold} D_{loss}\right)^2 K_{system}}{\left(K_{system}^2 + \left(\omega_{vold} D_{loss}\right)^2\right)^2}\right) \omega_{vold}^2 |x_{volder}|^2 \to 0 \quad \text{as } K_{system} \to \infty.$$

$$\tag{12}$$

It is also desirable to be able to predict the weld power $P_{e,\mathrm{avg}}^{\mathrm{weld}}$ for a new base structure with stiffness K_{system} after welding using the same weld assembly on a reference structure with stiffness $K_{system}^{\mathrm{ref}}$ drawing weld power $P_{e,\mathrm{avg}}^{\mathrm{weld,ref}}$. A simple linear relationship can be developed to provide a good approximation of the model in equation (11) away from the extreme stiffness regimes. The model is linearized at the inflection point $K_{system} = D_{loss}\omega_{weld}/\sqrt{3}$. The linear model can be expressed as follows for a small stiffness change $\delta K = K_{system} - K_{system}^{\mathrm{ref}}$:

$$\delta P = P_{e,avg}^{weld} - P_{e,avg}^{weld,ref} \approx \frac{3\sqrt{3}\omega_{weld}}{16} |x_{welder}|^2 \delta K. \tag{13}$$

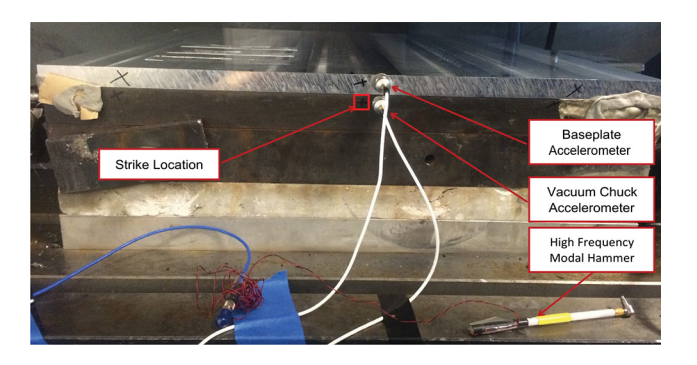
The slope of the linear fit in equation (13) does not depend on the damping coefficient D_{loss} . Therefore, if the weld power in a reference assembly is known, this linear relationship can be used to approximate the weld power for a different assembly without requiring an estimate for the damping coefficient.

4. Estimation of linear time invariant model parameters

4.1 Estimation of vacuum chuck stiffness

To model and quantify the relative contributions of the welded stack, baseplate and vacuum chuck fixture stiffnesses to the overall system's compliance defined in Figure 2(b), it is necessary to characterize the stiffness of the vacuum chuck anvil structure, which is the fixture used for all UAM welding experiments in this paper. Modal testing was carried out on the structure to estimate the dynamic stiffness of the structure near 20 kHz. The measurement is dynamic because mass, damping and stiffness influences are measured simultaneously in a single term. Figure 4 shows the setup for estimating the mechanical dynamic stiffness, where a high frequency impact hammer (PCB 086C80) is used to impart the excitation force, and two high frequency accelerometers (PCB 352A60) measure the vibration response. Accelerometers were chosen rather than a non-contact laser vibrometer because concurrent measurements of the baseplate and vacuum chuck were desired. The loading effect of the

Figure 4 Setup for modal hammer testing of the vacuum chuck anvil structure using a 9.53 mm (0.375 in) thick Al 6061-T6 baseplate. This test is used to measure the dynamic stiffness of the structure with impacts on the vacuum chuck



accelerometer coupled to the structure can be neglected, as the size and mass of the accelerometers are small compared to the size and mass of the base structure being measured. The PCB 352A60 accelerometer used has a resonant frequency of over 95 kHz, which is much higher than the frequency range of interest around 20 kHz. To emulate representative operating conditions in Section 5, a 9.53 mm (0.375 in) thick aluminum baseplate and a 3.18 mm (0.125 in) thick steel baseplate were each constrained to the chuck with vacuum pressure.

A QUATTRO signal analyzer was used to calculate frequency response functions (FRFs) $H(j\omega)$ between the force input and the corresponding measured acceleration output using 10 exponentially-windowed averages. The dynamic stiffness $\tilde{K}_{chuck}(j\omega)$ can be determined from the FRF $H_{chuck}(j\omega)$ between the force input F and the acceleration measured by the vacuum chuck accelerometer a_{chuck} to be:

$$\tilde{K}_{chuck}(j\omega) = H_{chuck}(j\omega)\omega^2,$$
 (14)

$$H_{chuck}(j\omega) = \frac{F}{a_{chuck}}(\omega).$$
 (15)

The transfer dynamic mechanical stiffness $K_{chuck}(j\omega)$ of the vacuum chuck with respect to each baseplate, estimated with

the strike location on the chuck and the response accelerometer location on the baseplate, is shown in Figure 5. The impedances measured with Al and steel baseplates mounted on the vacuum chuck are very close to each other. Ordinary coherence was close to 1 for the frequencies of interest near $20\,\mathrm{kHz}$. Dynamic stiffness values below $5\,\mathrm{kHz}$ are not plotted because the corresponding coherence was poor. As there are no resonant modes observed for the vacuum chuck anvil structure in the frequency range of interest near the welder frequency, it can be modeled as a lumped mechanical stiffness near $20\,\mathrm{kHz}$. The stiffness K_{chuck} of the lumped spring in Figure 2(b) is estimated to be $2\,\mathrm{GN/m}$ by taking the magnitude of the transfer dynamic mechanical stiffness of the chuck [equation (15)] near $20\,\mathrm{kHz}$.

4.2 Estimation of foil, stack and baseplate stiffnesses using finite element modeling

To estimate the combined stiffness of the foil, stack and baseplate, FEM in COMSOL Multiphysics is used. This estimated stiffness K_{FEM} is the equivalent stiffness of the foil (K_{foil}) , stack (K_{stack}) and baseplate (K_{base}) terms from equation (8). The simulations are quasi-static and for simplicity, all materials are assumed to remain in the elastic domain. In this paper, different alloys of aluminum, copper and steel are used for baseplate and foil materials. Built-in material properties in COMSOL for copper, Al 6063-T83 and AISI 4340 steel are used for simulation purposes. Although the alloying elements of these virtual materials differ from those in the materials tested, the linear elastic properties are the same.

The contact surface width is estimated to be 0.90 mm (0.035 in) using elastic Hertzian contact theory [2]. This contact width is used for all simulations in this study. Figure 6(a) shows the components of the finite element model. The normal load and transverse load from the welder are input as applied loads on the contact surface in the -z and y directions, respectively. The quasi-static stiffness is estimated by dividing the transverse applied load (2,000 N) by the average transverse displacement of the contact surface. Figure 6(b) shows the transverse (y-direction) deformation from the applied loads, which is used for estimating stiffness. A representative image of the graded mesh density of the FE model is shown in Figure 6(b). The inset illustrates the increased mesh density around the contact surface.

Figure 5 Dynamic transfer mechanical stiffness of the vacuum chuck with respect to a baseplate constrained to the vacuum chuck shown for aluminum and steel baseplates. Frequency response functions were measured by striking a modal hammer on the vacuum chuck and measuring the response using accelerometers on the vacuum chuck and the baseplate

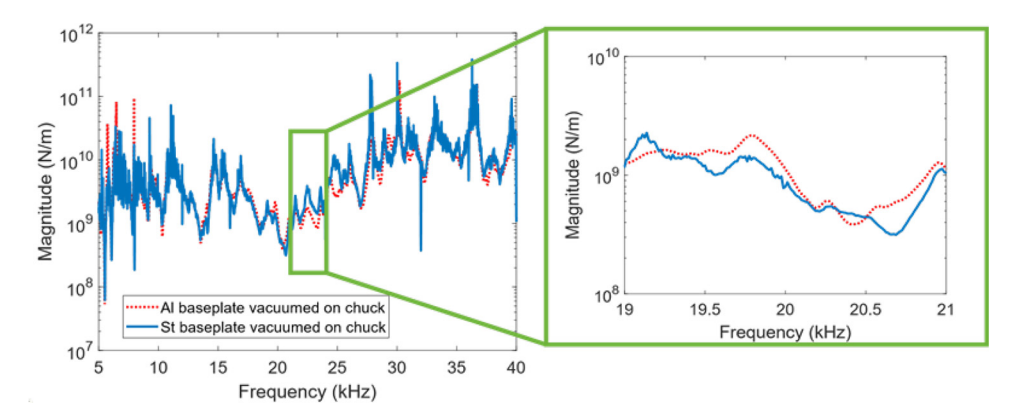
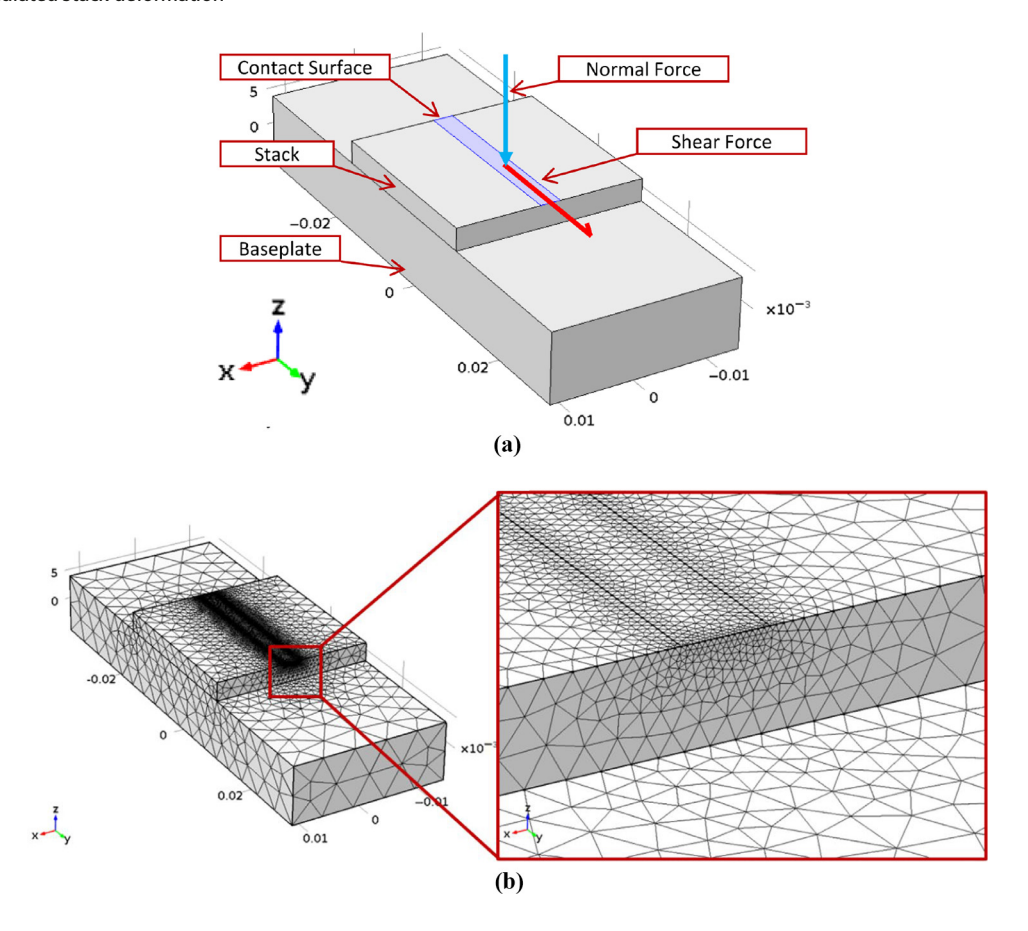


Figure 6 FE model of stack and baseplate: (a) contact surface used to apply the load from the weld tool. Normal (-z) and transverse (y) static loads are applied as traction loads on the contact surface; (b) Mesh density of FE model. A graded mesh was used near the contact surface to improve the accuracy of the simulated stack deformation



The combined stiffness of the foil, stack and baseplate (K_{FEM}) estimated in this section, and the stiffness of the vacuum chuck (K_{chuck}) estimated in Section 4.1, can together be used to estimate the system stiffness K_{system} using equation (8) as:

$$\frac{1}{K_{system}} = \frac{1}{K_{FEM}} + \frac{1}{K_{chuck}}.$$
 (16)

5. Experiments for validating weld power model

The model for weld power as a function of the system's compliance is established in equation (11). The system's compliance depends on the geometry and materials of the foil, previously welded layers, baseplate and the vacuum chuck fixture. The model also includes a damping parameter D_{loss} , which is calibrated in this section. Three studies are developed where the system's compliance is varied by changing the geometry and materials involved, and the resulting measurements of weld power are compared with model predictions to validate the weld power model. The compliance is estimated using the FE model and modal analysis as described in Section 4.

In Study A, the effect of baseplate stiffness on weld power is investigated. The baseplate materials and dimensions are

chosen to achieve a wide range of system stiffness values based on the FE model. In addition, the effect of build height on weld power is investigated for the welding of Al foil. Based on the findings in Hehr et al. (2016), it is expected that the weld power will decay with increasing build height. In Study B, the influence of foil stiffness on the change in weld power with build height is studied for the welding of Cu C11000-O60 foil. In contrast to the stack of aluminum foils, the FE model predicts that the system stiffness for a stack of copper foils welded onto an aluminum baseplate is not very sensitive to build height due to the higher elastic modulus of copper. In Study C, the effect of foil material on the damping parameter D_{loss} is investigated. In-situ weld power measurements during the welding of four foil materials with substantially different elastic moduli and yield strengths are compared with model predictions.

5.1 Study A: Effect of baseplate stiffness on weld power

The influence of baseplate stiffness on weld power in UAM is investigated by welding 20 layers of 2.54 cm (1.00 in) wide and 152 μm (0.006 in) thick Al 6061-H18 foil on steel and aluminum baseplates. To obtain a large contrast in system stiffness, a 9.53 mm (0.375 in) thick Al 6061-T6 baseplate and a 3.18 mm (0.125 in) thick annealed AISI 4130 steel baseplate were chosen. FE simulation results corresponding to 2-layer

and 20-layer Al 6061-H18 stacks welded onto these baseplates are shown in Figure 7. After the first foil is welded onto the baseplate, the system stiffness decreases from 433 to 364 MN/m (-16%) and 772 to 455 MN/m (-41%) for the Al and steel baseplates, respectively, during the welding of a 20-layer Al stack. The baseplate dimensions were chosen such that their masses are equal, which is important because some baseplate slip is present in UAM when a vacuum chuck fixture is used (Hehr, 2016). This intermittent slip may introduce mass loading effects on the welder so it is desirable for these potential mass loading effects to be equal. Al 6061-H18 weld foil was used because multiple layers can be welded without foil sticking to the sonotrode, known as nuggeting.

The weld parameters shown in Table 1 were selected based on previous work welding Al 6061-H18 onto steel in Wolcott (2015) and, hence, are different from the optimal values determined in a design of experiments study in Wolcott *et al.* (2014) for welding of Al 6061-H18 foil onto an Al 6061-T6 baseplate. Prior to welding, both baseplates were textured (welder rolled on a baseplate with ultrasonics on) using the weld parameters listed in Table 1.

Coefficients for the LTI model of the weld assembly were estimated using the procedure detailed in Hehr and Dapino (2017), which enables the estimation of the welder shear force from the vibration velocity and weld power measurements. The welder's vibration velocity was measured with a PSV-400 noncontact laser vibrometer at a sampling rate of 500 kHz and analyzed in the frequency domain with a block size of 8,192 points. The fundamental frequency of the velocity signal (welder frequency) was estimated as the frequency corresponding to the peak amplitude of the short-time Fourier transform of the signal with a frequency resolution of 9.5 Hz.

Figure 8 presents data for welding the second layer of aluminum foil using an aluminum baseplate versus a steel

Table 1 UAM weld parameters for welding Al 6061-H18 foil onto aluminum and steel baseplates

Vibration amplitude setpoint (peak-peak)	(μm)	22.0
Weld force	(N)	6,000
Welder travel speed	(m/min)	2.54
Baseplate temperature	(°C)	93.3

baseplate. It is shown that the welder frequency and welder's peak vibration velocity are nearly identical for both baseplates. On the other hand, the weld power and the estimated shear force are about 80% higher for the steel baseplate when compared to the Al baseplate. Weld power measurements and the corresponding simulated system stiffness values from the FE model are presented in Figures 9(a) and 9(b), respectively.

Parameter D_{loss} of the weld power model is calibrated based on weld power measurements for the 20-layer Al stack on the Al 6061-T6 baseplate. The squared errors between the weld power measurements and the model estimates are minimized using the fmincon routine in MATLAB to estimate D_{loss} to be 6,100 N.s/m. This value of D_{loss} is then substituted into the non-linear expression for weld power, equation (11), to predict the weld power in Figure 10 for the different build heights on the steel baseplate. The $|x_{welder}|$ term in equation (11) is calculated as $|x_{welder}| = |\dot{x}_{welder}|/\omega_{weld}$ for the fast Fourier transform magnitude of the welder's measured vibration velocity at the fundamental vibration frequency f_{weld} . For example, xwelder corresponding to welding of the second Al 6061-H18 layer on the aluminum baseplate is calculated to be $17.7 \,\mu\text{m}$. The decrease in displacement amplitude during welding is consistent with observations in Hehr and Dapino (2017). A similar reduction in displacement amplitude is observed in many power ultrasonic processes under high loads, as detailed in Ducharne et al. (2015).

Figure 7 FEA simulation of the UAM stack displacement for: (a) 2-layer and (b) 20-layer Al 6061-H18 stacks on a 9.53 mm (0.375 in) thick Al 6061-T6 baseplate with simulated $K_{system} = 433$ MN/m and 364 MN/m, respectively; (c) 2-layer and (d) 20-layer Al 6061-H18 stacks on a 3.18 mm (0.125 in) thick annealed AlSI 4130 steel baseplate with simulated $K_{system} = 772$ MN/m and 455 MN/m, respectively

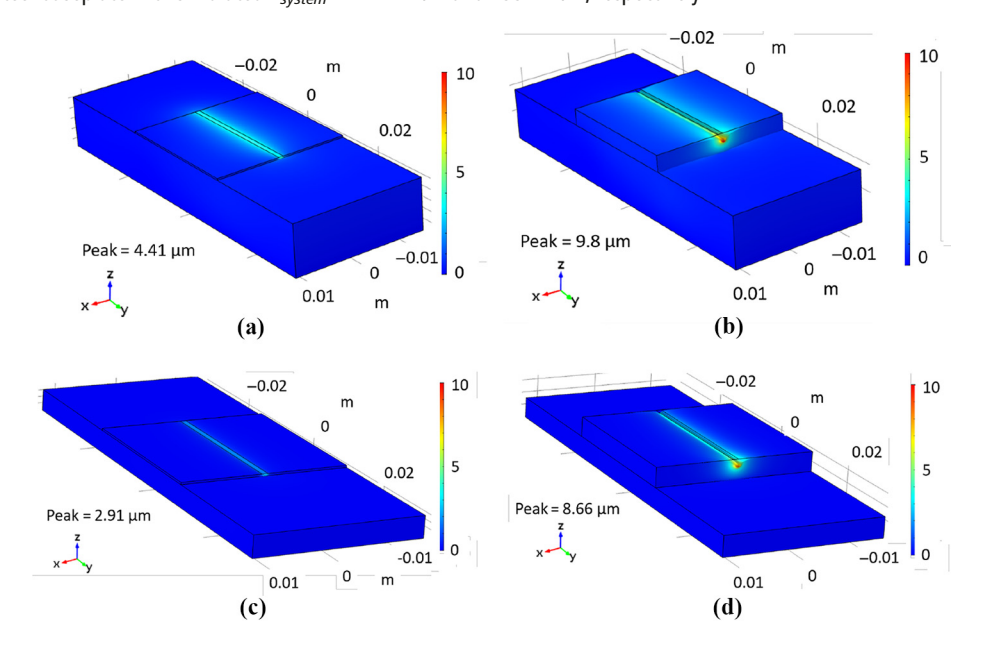


Figure 8 Comparison of in-situ measurements for welding the second layer of Al 6061-H18 foil with a 3.18 mm (0.125 in) thick annealed AlSI 4130 steel baseplate versus a 9.53 mm (0.375 in) thick Al 6061-T6 baseplate. The peak force (welder shear force) is estimated from the weld power and welder's vibration velocity measurements using the LTI model of the weld assembly. The steel baseplate weld required greater power to achieve the prescribed welder vibration amplitude

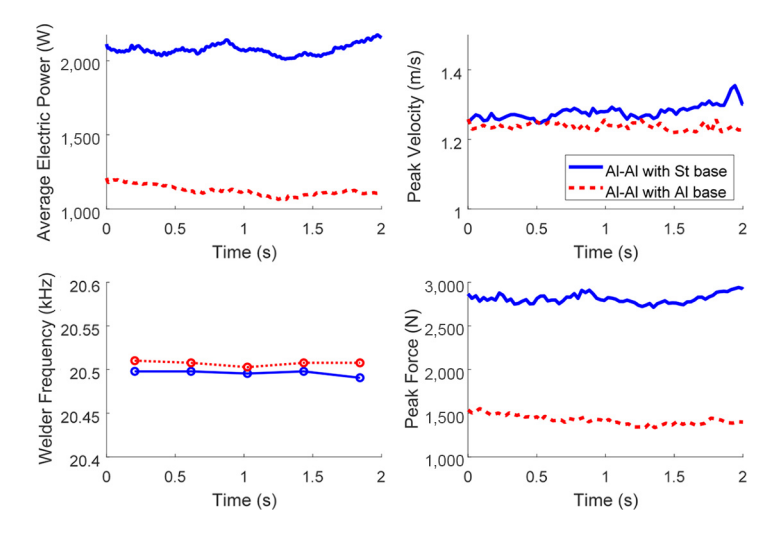
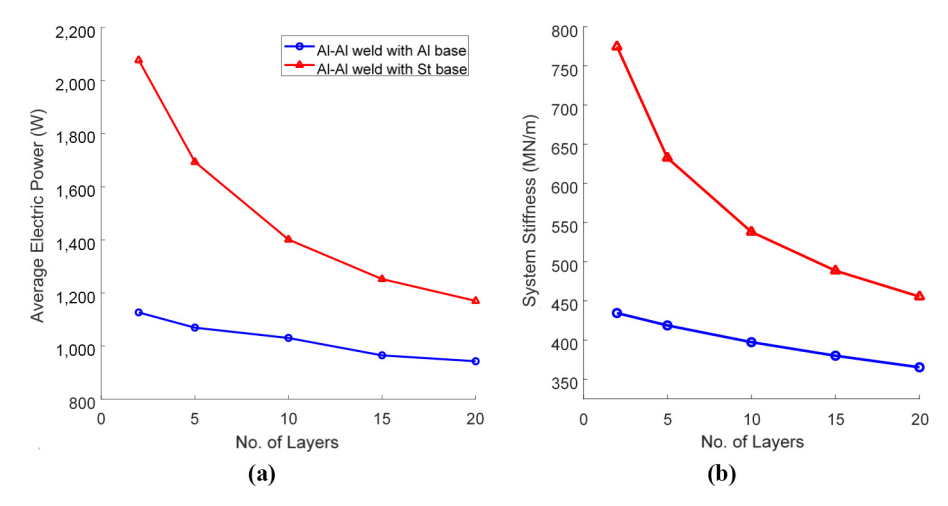


Figure 9 Trends in weld power and stiffness with build height for the welding of Al 6061-H18 foil: (a) measured average electric power; (b) simulated effective stiffness K_{system} from (16) based on FE modeled stiffness of the stack and baseplate



The vertical lines in Figure 10 indicate the range of system stiffness values attainable for foil to foil welding in UAM using our welding assembly with standard materials and geometries. Assuming steel and aluminum as the most and least stiff materials used, and our typical range of baseplate thicknesses, the minimum and maximum typical system stiffness values are evaluated to be 229 MN/m and 1,201 MN/m, respectively, using our vacuum chuck, shown in Figure 10.

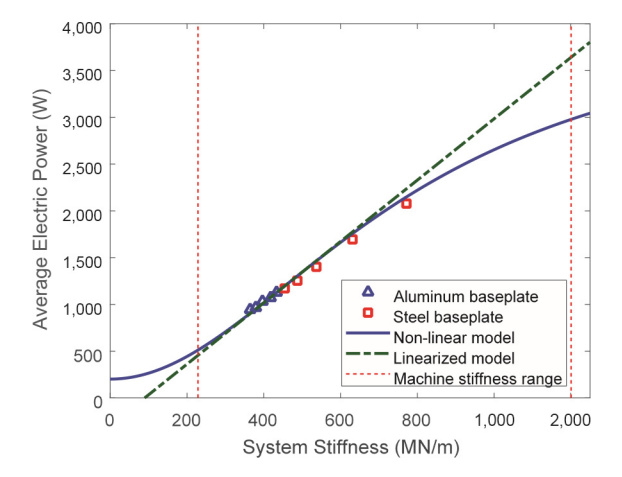
The non-linear model and experimental results in Figure 10 show good agreement. The non-linear [equation (11)] and the linearized [equation (13)] models have estimated R^2 values of 98% and 96%, respectively, relative to the experimental data. The error can be attributed to a few model assumptions. One assumption is that there is no slip between the welder and the foil being welded. From equation (13), this leads to the model overpredicting the weld power, which is supported by Figure 10.

The second assumption is that the contact width in UAM can be accurately estimated by Hertzian contact. Because of the plasticity inherent in UAM, the true contact width could be higher, which would change the predicted system stiffness. The agreement between the model and experiments indicates that weld power can be estimated if the welder's vibration amplitude and system stiffness are known after calibrating the model with a calibration data set. Moreover, because input weld power is related to consolidation quality, this expression can be used to select an amplitude setting for adequate bonding for a given baseplate and chuck setup.

5.2 Study B: Effect of foil material stiffness on weld power

The influence of foil material stiffness on weld power is investigated in this study. A stack of 10 copper foils are welded

Figure 10 Experimentally measured average electric power plotted against the system stiffness estimated from the model for a 0.9 mm contact width. Data points for each baseplate are calculated from welds on consecutive layers, with progressively decreasing stiffness with build height. The non-linear model uses (11) and the linearized model uses (13) to estimate the average electric power, with parameter D_{loss} determined to be 6,100 N.s/m from weld power data while welding the second Al 6061-H18 layer on the aluminum baseplate. The vertical lines show the range of system stiffness values expected for foil-to-foil welding using our welding setup



onto a 9.53 mm (0.375 in) thick Al 6061-T6 baseplate using the weld parameters listed in Table 2, shown in Figure 11. The corresponding system stiffness values as a function of build height, estimated from the FE model, are shown in Figure 12(a). The stack was built using copper as the foil material because the estimated system stiffness does not significantly decrease with build height (less than 2% reduction for 10 layers), in contrast to about a 9% reduction for 10 layers of aluminum as the foil material. The stiffness values for a 2-layer Cu build are 11% higher than a corresponding 2-layer Al build on an Al 6061-T6 baseplate with the same thickness. A different sonotrode and transducer assembly was used for the work in Section 5, with different LTI model parameters and, hence, different power-amplitude relationships.

The weld parameters shown in Table 2 were selected for good bonding, which means that the foil could not be peeled off by hand and there was no welding of copper to the sonotrode (nuggeting). The resulting weld power measurements are shown in Figure 12(b). The mean weld power values for the first 10 layers are within 5% of each other. This study validates the hypothesis that system stiffness is the controlling variable for weld power at fixed process conditions. The D_{loss} value determined from Study A (6,100 N.s/m) is used to estimate the weld power from equation (11). Although the D_{loss} value was

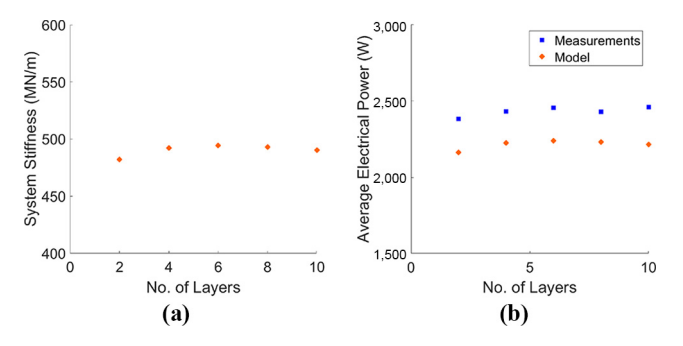
Table 2 UAM weld parameters for welding 10 layers of Cu C11000-060 on an aluminum baseplate

Vibration amplitude setpoint (peak-peak)	$(\mu{\sf m})$	32
Weld force	(N)	6,000
Welder travel speed	(m/min)	5.08
Baseplate temperature	(°C)	25

Figure 11 10-layer stack of Cu C11000-060 foil welded onto a 9.53 mm (0.375 in) thick Al 6061-T6 baseplate



Figure 12 Weld power and system stiffness values for welding 10 layers of 0.152 mm (0.006 in) thick C11000 foil onto a 9.53 mm (0.375 in) thick Al 6061-T6 baseplate: (a) simulated effective stiffness K_{system} from (16) based on FE modeled stiffness of the stack and baseplate; (b) measured average electric power compared against predictions from the weld power model in equation (11)



determined for Al-Al welding, the model power estimates are within 10% of the weld power measurements. It is hence proposed that the damping parameter is independent of the foil material used, and this proposition is tested more rigorously in Study C for UAM with four different foil materials welded under the same process conditions.

5.3 Study C: Effect of foil material on model damping parameter

The influence of foil material properties on weld power in the UAM process was studied by welding 2.54 cm (1.00 in) wide and 152 μ m (0.006 in) thick Al 6061-H18, Al 6061-O, Al 3003-H18 and Cu C11000-O60 foils onto an Al 6061-T6 baseplate with the same peak-peak weld amplitude setpoint, weld force and welder travel speed. These foils were chosen because they have substantial differences in their elastic moduli and yield strengths, which would affect the elastic and plastic response of the foil material during welding. Mechanical properties for Al 6061-O and Al 3003-H18 were obtained from the ASM materials handbook (ASM Handbook Committee, 1990) for the respective alloy and temper combinations. As the

properties were not available in the literature, tensile properties for Al 6061-H18 and Cu C11000-O60 were measured by testing the foils in uniaxial tension using an MTS load frame with a digital image correlation system for strain measurements. Samples were prepared and tested following the ASTM E8/E8M standards (ASTM International, 2021) for sheet-type specimens. Table 3 summarizes the strength, stiffness and elongation values for each foil material. The system stiffness for two layers of aluminum and copper foil welded on a 9.53 mm (0.375 in) thick aluminum baseplate ($K_{FEM,Al}$) are computed using equation (16) and summarized in Table 4. The copper weld foils have a higher system stiffness value because of their higher elastic modulus.

Identical weld parameters were used to weld all of the foil types listed in Table 3 onto the same 9.53 mm (0.375 in) thick Al 6061-T6 baseplate, held in place on the CNC table using a vacuum chuck. Statistical techniques (analysis of variance) have been used in Wolcott et al. (2014) to demonstrate that weld force does not significantly influence weld quality in UAM of Al 6061; hence, it was fixed at a typical value of 6,000 N. The travel speed of the welder was also fixed at a typical value of 5.08 m/min (200 in/min). Two layers of each foil type were welded onto the baseplate one at a time. The first foil of all foil types was welded onto the baseplate using a 32 μ m peak-peak weld amplitude setpoint, which was found to produce qualitatively acceptable welds for all of the foil types. A weld was considered to be acceptable if the welded foil could not be pulled off by hand. To understand the interrelation between the weld foil type and the UAM process, the welder's vibration amplitude and average weld power were measured in situ during the welding of the second foil.

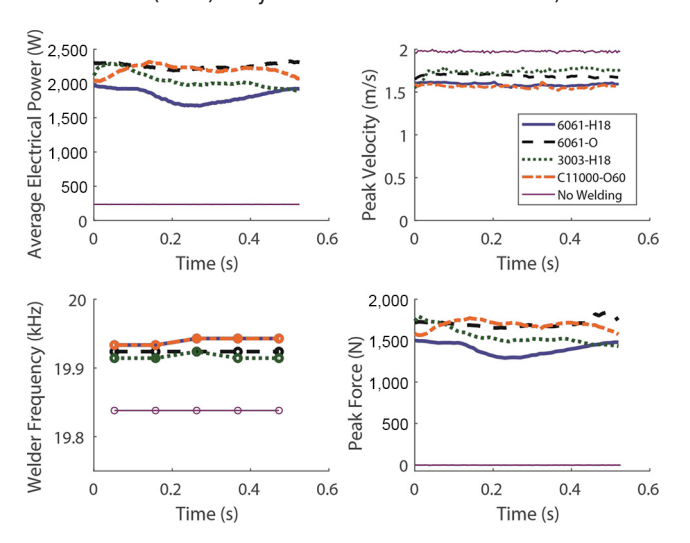
In Figure 13, the average electric power, peak vibration velocity, excitation frequency and estimated shear force for the $32 \,\mu$ m peak-peak weld amplitude setpoint case are close to one another for all of the foil types. All of the data sets for welding cases are substantially different than those for actuating the welder under no load, which is consistent with earlier work in Hehr and Dapino (2017). The similarities between the foils in Figure 13 are somewhat unexpected due to the large differences in foil strengths. For example, Al 6061-O has about a quarter of the tensile yield strength of Al 6061-H18, but draws about the same electrical power from the welder during welding of the second foil. Hence, we propose that weld power is mainly determined by the elastic compliance of the foil, workpiece and fixture.

The second foil was welded onto the first foil using the range of peak-peak weld amplitude setpoints specified in Table 5. The span of values was chosen to provide a wide range of weld power and study both successful and unsuccessful foil-to-foil bonding. For example, no bonding was observed when attempting to weld the second foil of all foil types at the $12 \, \mu m$

Table 4 Influence of foil and baseplate material on effective system stiffness (K_{system}) for 2 layers of foil welded onto a 9.53 mm (0.375 in) thick Al 6061-T6 baseplate. Stiffness units are (MN/m)

Foil material	K _{chuck}	K _{FEM}	K _{system}
Aluminum	2,000	555	433
Copper	2,000	636	483

Figure 13 Measurements during welding of different metal foil types onto one another, i.e. foil to foil results and the reference no welding condition. The first foil was welded onto a 9.53 mm (0.375 in) thick Al 6061-T6 baseplate. The power, peak velocity, frequency and peak shear force profiles are similar in magnitude for all of the foil types. The welder frequency estimates for Al 6061-H18 and Cu C11000-O60 data overlap. Measurements are shown in the steady-state regions of the welds (at least 12.7 mm (0.5 in) away from start and end of each weld)



peak-peak weld amplitude setpoint. The copper foil failed to bond successfully even at the 16 μ m peak-peak weld amplitude setpoint. All of the foil types exhibit qualitative characteristics of good welds at the 32 μ m peak-peak weld amplitude setpoint, shown in Figure 14.

It is known that weld power and peak-peak weld amplitude setpoint have a quadratic relationship under no load (Hehr and Dapino, 2017). Modeling the welder's coupling with the materials being welded as a generalized dynamic mechanical stiffness, it is shown in equation (7) that the quadratic relationship holds even under load if the damping parameter is considered to be independent of weld amplitude, which is supported by the good fit between model predictions of weld power and the measured weld power in Figure 15(a) for all of the foil types. The D_{loss}

Table 3 Summary of foil tensile properties

Tensile property	Units	Al 6061-H18	Al 6061-0	Al 3003-H18	Cu C11000-060
Elastic modulus	(GPa)	71	69	69	106
Yield strength	(MPa)	237	55	185	107
Ultimate strength	(MPa)	246	125	200	228
Elongation	(%)	3	25	4	25

Table 5 UAM weld parameters for welding the second layer of all foil types with an Al 6061-T6 baseplate

Vibration amplitude setpoint (peak-peak)	(μm)	12, 16, 20,, 32
Weld force	(N)	6,000
Welder travel speed	(m/min)	5.08
Baseplate temperature	(°C)	25

Figure 14 Welded foils along with ultimate tensile strength (UTS) for reference. Two layers of each material were welded onto a 9.53 mm (0.375 in) thick Al 6061-T6 baseplate. Welds using a 32 μ m peak-peak weld amplitude setpoint are shown here

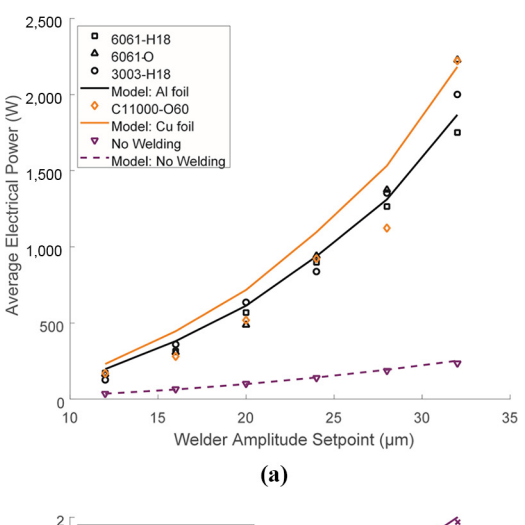


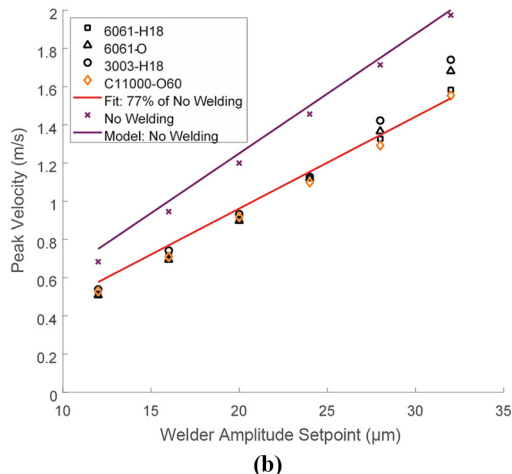
parameter determined from Study A (6,100 N.s/m) and the peak velocity measurement during welding are used to estimate the weld power from equation (11). The agreement between model and experiment also supports our proposition that the mechanical strength of the foil material does not significantly affect the weld power for foil-to-foil welding. It is also observed from Figure 15(a) that the weld power-amplitude relationship is not strongly affected by whether successful foil-to-foil bonding is achieved.

Based on the findings in Section 5.3, we develop a procedure to determine the amplitude setpoint required to achieve a target weld power for different build configurations. It is necessary to estimate the vibration amplitude of the welder under load as a function of the amplitude setpoint to use in equation (11). A linear regression model is developed between the peak velocity for the no welding cases and the peak velocity for welding all the foils, assuming zero Y-intercept. Using the method of least squares, the best-fit slope of the model is found to be 0.77, and the best-fit regression line is shown in Figure 15(b).

The weld power model in equation (11) is combined with the following simplifying assumptions, namely, the welder's vibration amplitude under load is 77% of the amplitude under no load; the frequency shift due to welding is small compared to the ringing frequency, hence $\omega_{weld} \approx \omega_{ring}$; the value estimated for parameter D_{loss} in this study (6,100 N.s/m) applies to other UAM systems. Hence, the amplitude setpoint to achieve the target power is calculated from equation (11) to be

Figure 15 Measurements for attempting welding of different metal foil types onto one another, i.e. foil to foil results for welding the second foil to the first foil and the no welding (actuated in air) condition for reference over a range of peak-peak weld amplitude setpoints. Model predictions are computed using the system stiffnesses of Al and Cu builds from Table 4 in equation (11). (a) Average electric power calculated by averaging the power measurements in the steady-state region of the weld (at least 12.7 mm (0.5 in) away from both the start and end of the weld). (b) Peak velocity of the vibration of the welder during welding and in air (no welding). The regression line between the peak velocity data in the no-welding cases and welding all the foils is shown. The least squares estimate of the slope value is 0.77, with an R^2 value of 98%





$$|x_{welder}| = \frac{1}{0.77\omega_{ring}} \sqrt{\frac{2P_{e,avg}^{weld}}{\left(D_t + D_{loss} \frac{K_{system}^2 + (\omega_{ring}D_{loss})^2}{K_{system}^2 + (\omega_{ring}D_{loss})^2}\right)}.$$
(17)

Relationship [equation (17)] serves as a tool to determine process settings to achieve a target power level with UAM for different workpiece and fixture combinations. For a different UAM system, the parameters D_t and D_{loss} would have to be calibrated according to the procedure described in Hehr and Dapino (2017). As power has been shown to strongly influence weld quality (Hehr *et al.*, 2016),

this tool saves the UAM user from costly and time-consuming trial welds and testing to tune weld parameters. For example, if one determines that approximately 3,000 W of average electric power is required to produce a strong bond between two metal foils, the target weld power and the estimated system stiffness for a given workpiece and fixture can be substituted into equation (17) to estimate the welder amplitude setpoint required to achieve the target weld power and weld quality.

6. Conclusions

A lumped parameter LTI model of the UAM welder coupled to the materials being welded during UAM has been developed to predict the weld power at a given weld amplitude as a function of the overall system's compliance, considering the contributions of the foil material being welded, the workpiece being welded onto and the fixture. The non-linear relationship between weld power and system stiffness has been presented, along with a linearized relationship that has been shown to provide a good approximation. Prior to this study, predictive relations for UAM weld power have not been successfully developed.

Modal analysis and FEM are used to estimate the different component compliances, and an equivalent circuit model is used to describe the overall system's compliance, which is then used to compute the weld power for a given weld amplitude setting. The model shows good agreement with measurements for a variety of build and fixture configurations tested: up to 20 layers of Al welded onto baseplates with different stiffnesses; up to 10 layers of Cu welded onto an Al baseplate; and 2-layer builds with different alloys and tempers of Al and Cu foil. Model predictions of higher weld power for stiffer (lower compliance) builds agree with experimental data. Weld power is also found to be largely insensitive to foil type (and hence, foil strength) within the Al foils, although different welder effort is required to satisfactorily weld different foil types. A framework has been developed to determine the weld amplitude setpoint to obtain a target weld power for a given build configuration.

These observations support the conclusion that the elastic compliance of the system has the most dominant influence on weld power. This modeling framework, using a calibrated damping coefficient, can predict the weld amplitude required to reach a certain target weld power for different welder, workpiece and fixture designs. This reduces the need for time-consuming pilot weld studies for new UAM build materials, configurations and systems.

Notes

- 1 Measurements of the CNC table motion during welding using the laser vibrometer showed that the velocity magnitude of the CNC table is less than 5% of the velocity magnitude of the vacuum chuck.
- 2 The contact width is estimated using closed-form equations for a cylinder on a flat surface (Bhushan, 2013).

References

ASM Handbook Committee (1990), ASM Handbook Vol. 2 Properties and Selection: Nonferrous Alloys and Special-Purpose

- Materials, ASM International, Materials Park, OH, doi: 10.31399/asm.hb.v02.9781627081627.
- ASTM International (2021), E8/E8M-21 Standard Test Methods for Tension Testing of Metallic Materials, West Conshohocken, PA, available at: https://doi-org.proxy.lib.ohio-state.edu/10.1520/E0008_E0008M-21
- Bhushan, B. (2013), "Contact between solid surfaces", *Introduction to Tribology*, John Wiley and Sons Ltd., West Sussex, doi: 10.31399/asm.hb.v02.9781627081627.
- de Silva, C.W. (2007), Vibration Damping, Control, and Design, CRC Press, doi: 10.1201/9781420053227.
- Diez, E., Leal-Muñoz, E., Perez, H. and Vizan, A. (2017), "Dynamic analysis of a piezoelectric system to compensate for workpiece deformations in flexible milling", *Mechanical Systems and Signal Processing*, Vol. 91, pp. 278-294, doi: 10.1115/1.2831039.
- Ducharne, B., Guyomar, D., Sébald, G. and Zhang, B. (2015), "Modeling energy losses in power ultrasound transducers", *Power Ultrasonics*, Elsevier, pp. 241-256. 10.1016/B978-1-78242-028-6.00010-7.
- Friel, R.J. (2015), "Power ultrasonics for additive manufacturing and consolidating of materials", *Power Ultrasonics*, Elsevier, pp. 313-335, doi: 10.1016/B978-1-78242-028-6.00013-2.
- Gibert, J.M., Austin, E.M. and Fadel, G. (2010), "Effect of height to width ratio on the dynamics of ultrasonic consolidation", *Rapid Prototyping Journal*, Vol. 16 No. 4, pp. 284-294, doi: 10.1108/13552541011049306.
- Graff, K., Short, M. and Norfolk, M. (2010), "Very high power ultrasonic additive manufacturing (VHP UAM) for advanced materials", *Proceedings of the Solid Freeform Fabrication Symposium*, Austin, TX.
- Graff, K., Short, M. and Norfolk, M. (2011), "Very high power ultrasonic additive manufacturing (VHP UAM)", *Proceedings of the Solid Freeform Fabrication Symposium*, *Austin*, TX.
- Han, T., Kuo, C.H., Sridharan, N., Headings, L., Babu, S.S. and Dapino, M.J. (2020), "Effect of preheat temperature and post-process treatment on the microstructure and mechanical properties of stainless steel 410 made via ultrasonic additive manufacturing", *Materials Science and Engineering: A*, Vol. 769, p. 138457, doi: 10.1016/j.msea.2019.138457.
- Hehr, A. (2016), "Process control and development for ultrasonic additive manufacturing with embedded fibers", PhD thesis, The Ohio State University, Columbus, OH.
- Hehr, A. and Dapino, M.J. (2017), "Dynamics of ultrasonic additive manufacturing", *Ultrasonics*, Vol. 73, pp. 49-66, doi: 10.1016/j.ultras.2016.08.009.
- Hehr, A., Wolcott, P.J. and Dapino, M.J. (2016), "Effect of weld power and build compliance on ultrasonic consolidation", *Rapid Prototyping Journal*, Vol. 22 No. 2, pp. 377-386, doi: 10.1108/rpj-11-2014-0147.
- Kong, C.Y., Soar, R.C. and Dickens, P.M. (2004), "Optimum process parameters for ultrasonic consolidation of 3003 aluminium", *Journal of Materials Processing Technology*, Vol. 146 No. 2, pp. 181-187, doi: 10.1016/j. jmatprotec.2018.02.001.
- Obielodan, J.O., Ceylan, A., Murr, L.E. and Stucker, B.E. (2010), "Multi-material bonding in ultrasonic consolidation", *Rapid Prototyping Journal*, Vol. 16 No. 3, pp. 180-188, doi: 10.1108/13552541011034843.

- Sridharan, N., Wolcott, P.J., Dapino, M.J. and Babu, S.S. (2016), "Microstructure and texture evolution in aluminum and commercially pure titanium dissimilar welds fabricated using ultrasonic additive manufacturing", *Scripta Materialia*, Vol. 117, pp. 1-5, doi: 10.1016/j.scriptamat.2016.02.013.
- Sriraman, M.R., Gonser, M., Fujii, H.T., Babu, S.S. and Bloss, M. (2011), "Thermal transients during processing of materials by very high power ultrasonic additive manufacturing", *Journal of Materials Processing Technology*, Vol. 211 No. 10, pp. 1650-1657, doi: 10.1016/j. jmatprotec.2011.05.003.
- Wang, Z.Y. and Rajurkar, K.P. (1996), "Dynamic analysis of the ultrasonic machining process", *Journal of Manufacturing Science and Engineering*, Vol. 118 No. 3, pp. 376-381, doi: 10.1115/1.2831039.
- White, D. (2003), "Ultrasonic consolidation of aluminum tooling", *Advanced Materials and Processes*, Vol. 161, pp. 64-65.
- Wiercigroch, M., Neilson, R.D. and Player, M.A. (1999), "Material removal rate prediction for ultrasonic drilling of

- hard materials using an impact oscillator approach", *Physics Letters A*, Vol. 259 No. 2, pp. 91-96, doi: 10.1016/s0375-9601(99)00416-8.
- Wolcott, P.J., Hehr, A. and Dapino, M.J. (2014), "Optimized welding parameters for Al 6061 ultrasonic additive manufactured structures", *Journal of Materials Research*, Vol. 29 No. 17, pp. 2055-2065, doi: 10.1557/jmr.2014.139.
- Wolcott, P.J. (2015), "Ultrasonic additive manufacturing: Weld optimization for aluminum 6061, development of scarf joints for aluminum sheet metal, and joining of high strength metals", PhD thesis, The Ohio State University, Columbus, OH.
- Yi, D., Zhang, S., Zhang, H., Zheng, L. and Norfolk, M. (2017), "Power consumption and friction coefficient in the ultrasonic consolidation of aluminium alloys", *Materials Science and Technology*, Vol. 33 No. 6, pp. 744-750, doi: 10.1080/02670836.2016.1254912.

Corresponding author

Marcelo J. Dapino can be contacted at: dapino.1@osu.edu